Within- and Between-Event Variabilities of Strong-Velocity Pulses of Moderate Earthquakes within Dense Seismic Arrays

Ming-Hsuan Yen[*,1,2] , Sebastian von Specht[3,4] , Yen-Yu Lin[3,5] , Fabrice Cotton[1,2] , and Kuo-Fong Ma[3,4,5]

ABSTRACT

Ground motion with strong-velocity pulses can cause significant damage to buildings and structures at certain periods; hence, knowing the period and velocity amplitude of such pulses is critical for earthquake structural engineering. However, the physical factors relating the scaling of pulse periods with magnitude are poorly understood. In this study, we investigate moderate but damaging earthquakes (M_w 6–7) and characterize ground-motion pulses using the method of Shahi and Baker (2014) while considering the potential static-offset effects. We confirm that the within-event variability of the pulses is large. The identified pulses in this study are mostly from strike-slip-like earthquakes. We further perform simulations using the frequency–wavenumber algorithm to investigate the causes of the variability of the pulse periods within and between events for moderate strike-slip earthquakes. We test the effect of fault dips, and the impact of the asperity locations and sizes. The simulations reveal that the asperity properties have a high impact on the pulse periods and amplitudes at nearby stations. Our results emphasize the importance of asperity characteristics, in addition to earthquake magnitudes for the occurrence and properties of pulses produced by the forward directivity effect. We finally quantify and discuss within- and between-event variabilities of pulse properties at short distances.

KEY POINTS

- We investigate ground-motion pulses of recent moderate earthquakes, taking into account static-offset effects.
- We quantify and discuss within- and between-event pulses variabilities properties at short distances.
- Simulations reveal that the asperity properties have a strong influence on the pulse features.

Supplemental Material

INTRODUCTION

Near-fault ground motion with strong-velocity pulses can cause significant damage to nearby structures at certain periods. The period and the amplitude of strong-velocity pulses are, therefore, especially critical for earthquake structural engineering, and several studies have recently incorporated the effects of pulse-like motions in ground-motion prediction models or probabilistic seismic hazard analysis (Shahi and Baker, 2011; Almufti et al., 2015; Tarbali et al., 2019). Chioccarelli and Iervolino (2013) analyzed the disaggregation and design scenarios for near-source possibilistic seismic hazard analysis, and showed the large impacts of pulses and forward directivity effects on the final results. Most studies assume that pulse periods scale with earthquake magnitude, and then use empirical relationships relating pulse periods and earthquake magnitudes (Somerville, 2003; Chioccarelli and Iervolino, 2010; Shahi and Baker, 2011, 2014), as shown in Figure 1. However, these empirical relationships show that the pulse periods are highly variable from one earthquake to another of similar magnitude (between-event variability) or even for various records of a single earthquake (within-event variability). Several studies have indeed suggested that additional source parameters may impact upon the pulse periods. Mena and Mai (2011) advocated that pulse periods may be related to the total area of the asperities associated with a fault
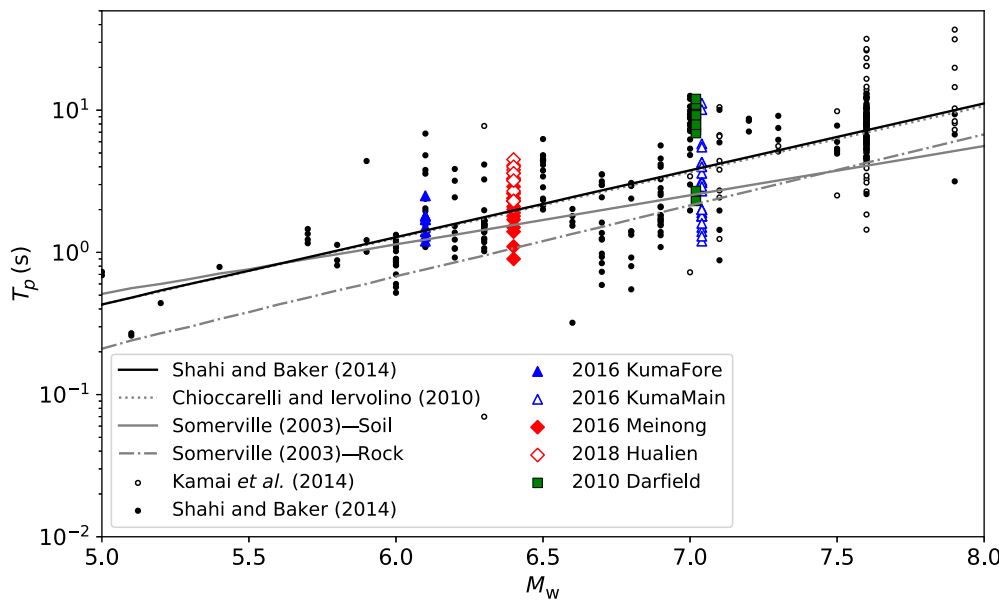
Figure 1. Values of the pulse period, T_p, as a function of earthquake moment magnitudes. The extracted pulse period with static-offset removal from this study, presented by symbols, are shown together with other studies of Kamai *et al.* (2014) and Shahi and Baker (2014), which have not been considering the static-offset removal. The black-solid line indicates the regression of Shahi and Baker (2014), which calibrated the earthquake ground-motion records from the Next Generation Attenuation (NGA)-West2 database (Ancheta *et al.*, 2013). The gray-dotted line indicates the regression of Chioccarelli and Iervolino (2010), which calibrated the data from NGA database that includes all types of faulting events with **M** 5.2–7.5. The gray-solid line indicates the regression of Somerville (2003) for soil site that calibrated the data from all faulting types events with **M** 6.7–7.6. The gray-dashed-dotted line indicates the regression of Somerville (2003) for rock site that calibrated the data from all faulting types events with **M** 6.1–7.4. Black dots represent 244 recordings classified as the pulses from the NGA-West2 database (Ancheta *et al.*, 2013) in the study of Shahi and Baker (2014). Open circles represent the fling-step pulses published by Kamai *et al.* (2014). The color version of this figure is available only in the electronic edition.

phenomena that the pulses result from. Indeed, the near-source effects affecting the pulse characteristics are not only due to the forward directivity, because static offsets (fling-step effect) may also create pulses (Somerville *et al.*, 1997; Dreger *et al.*, 2011; Baltzopoulos *et al.*, 2020). Past analyses of fling steps (e.g., Kamai *et al.*, 2014) were mostly performed for large-magnitude earthquakes and showed that the fling steps were mostly in the large-magnitude earthquake (Fig. 1).

High-quality data and dense seismological networks offer an opportunity to better understand near-fault ground motion and strong-velocity pulses. We investigate the variability of pulses and the factors controlling this variability through the analysis of observations from recent earthquakes and simulations. We analyze mainly earthquakes (M_w 6–7) that have occurred over the past decade and for which we have high-quality near-fault data, namely two Taiwanese earthquakes, two Japanese earthquakes, and one New Zealand earthquake, as summarized in Table 1.

Various methods for identifying and classifying pulses have been developed over recent decades (Mena and Mai, 2011; Hayden *et al.*, 2014; Shahi and Baker, 2014; Chang *et al.*, 2016; Sharbati *et al.*, 2020). Mena and Mai (2011) used a spectrogram analysis to detect pulses and classified the directivity pulses based on a specified energy level. Sharbati *et al.* (2020) reviewed the methods for velocity pulse identification and classification,

and a geometrical directivity parameter. Cork *et al.* (2016) claimed that pulse periods might be associated with the tectonic regime or stress drop. Fayjaloun *et al.* (2017) found that the pulse period is sensitive to the rupture length toward the stations.

The physical factors controlling between- and within-event variabilities of pulses' amplitudes and periods are, therefore, still poorly understood. To our knowledge, few studies have analyzed pulses from moderate earthquakes' ground motions in a systematic way by trying to separate the physical

TABLE 1
Summary of the Parameters of the Earthquakes Considered in This Work

Event	UTC Time (yyyy/mm/dd hh:mm:ss)	Epicenter	Focal Depth (km)	Strike and Dip	Rake	M_w	Faulting Type
Kumamoto foreshock	2016/04/14 12:26:36	32.7417° N, 130.8087° E	11.39	205° and 74°	180°	6.1	Strike slip
Kumamoto mainshock	2016/04/15 16:25:06	32.7545° N, 130.7630° E	12.45	205° and 72°	−142°	7.04	Strike slip
				235° and 65°	−142°		Strike slip
Meinong	2016/02/05 19:57:27	22.92° N, 120.54° E	14.6	295° and 22°	20°	6.4	Strike-slip like
Hualien	2018/02/06 15:50:43	24.132° N, 121.659° E	10.6	216° and 56°	26°	6.4	Oblique slip
Darfield	2010/09/03 16:35:46	−43.6148° N, 172.0386° E	10.84	85° and 82°	154°	7.02	Strike slip

and proposed a method, which is based on the asymmetric Gaussian Chirplet model, adapted dictionary-free orthogonal matching pursuit algorithm, and the Newton method, for the detection and extraction of velocity pulses. In the following and in order to be consistent with other pulse analysis studies (e.g., Shahi and Baker, 2014), we employ the wavelet analysis of Shahi and Baker (2014) that can extract and characterize the strongest pulses at arbitrary orientations in multicomponent ground motions.

In this study, we aim to understand the potential factors driving the directivity effect (e.g., asperity properties) and to develop a strategy to remove the impact of the static-offset effect from near-fault ground motion. We first clarify the impact of static offsets on pulse characteristics by removing the static offsets from all the recordings and then analyze only pulses created by the directivity effect of the dynamic motion. We further perform frequency–wavenumber simulations (Zhu and Rivera, 2002) to investigate the within- and between-event variabilities of these moderate earthquakes. We test different fault dips and the impact of different asperity locations and sizes. We finally discuss the within- and between-event variabilities of pulse periods that need to be considered for engineering applications.

STRONG-VELOCITY PULSES FROM OBSERVATIONS
Earthquakes and data

Our studies of the damage arising from moderate earthquakes due to strong-velocity pulses have been motivated by the 2016 Meinong and 2018 Hualien earthquakes, which caused serious damage to nearby buildings in Taiwan. It was suggested that strong-velocity pulses were responsible for the observed damage (Kanamori et al., 2017; Lin et al., 2018; Kuo, Huang, et al., 2019; Ji et al., 2019; Lin et al., 2020). The 2016 M_w 6.4 Meinong earthquake struck southwest Taiwan and was associated with a low-angle strike-slip blind fault dipping toward to north (Fig. 2a; Lee et al., 2016). The focal depth was 14.6 km, according to the Central Weather Bureau (CWB) report. There were two asperities in this event, and the strong-velocity pulses were more associated with the larger one (Lin et al., 2018). The 2018 M_w 6.4 Hualien earthquake ruptured several fault segments offshore (Lee et al., 2019), but the damaging motion was mostly related to the onshore Milun fault, which is a nearly vertical strike-slip fault at a shallow depth (Lin et al., 2020). The main asperity is located near the inland segment of the Milun fault, and strong-velocity pulses were mostly related to this segment (Fig. 2b). As such, we consider only onshore segment of the Milun fault to compute the rupture distance for analysis of the strong-velocity pulses.

We use the waveform data provided by the Taiwan Strong Motion Instrumentation Program (TSMIP) network of the CWB of Taiwan (Liu et al., 1999) for these two earthquakes. The records were downloaded from the database of near-fault strong motions with pulse-like velocity in Taiwan (Kuo, Chao, et al., 2019). The acceleration waveform data consist of three components with a sampling rate of 200. The instrument response is flat and the response range is from direct current to 50 Hz (Liu et al., 1999; Liu and Tsai, 2005).

To understand the features of the strong-velocity pulse, in addition to the Taiwanese events, we extend our studies to the Kumamoto, Japan, earthquake sequence and the Darfield, New Zealand, earthquake. These were moderate earthquakes, with high-quality near-field strong-motion data available.

The 2016 Kumamoto earthquake sequence that hit southwest Japan also generated significant velocity pulses (Somei et al., 2020). The second foreshock (M_w 6.1) ruptured along the northern part of the Hinagu fault, which is a nearly vertical fault (Kobayashi et al., 2017). The 2016 M_w 7.0 Kumamoto mainshock ruptured along the intersecting Futagawa and Hinagu faults. We use the waveform data provided by the strong-motion networks, K-Net and KiK-Net, of the National Research Institute for Earth Science and Disaster Resilience, and the strong-motion network of the Japanese Meteorological Agency for these two Japanese earthquakes. The acceleration waveform data consist of three components with a sampling rate of 100 Hz. The instrument response is again flat and with zero-phase below 10 Hz, and only a gain correction is applied.

The 2010 M_w 7.02 Darfield earthquake struck the South Island of New Zealand on a strike-slip fault. The epicenter was located 40 km west of Christchurch near the town of Darfield, and the focal depth was about 10 km. It was caused by a previously unknown regional right-lateral strike-slip fault in the western section of the Canterbury plains, later named the Greendale fault. This earthquake was also well recorded by the GNS strong-motion network with high-quality waveform data. The acceleration waveform data consist of three components from different instruments with various sampling rates and the instrument responses. The waveforms have been processed by GNS Science for the GNS strong-motion database (Houtte et al., 2017).

Methodology

We apply the wavelet analysis algorithm of Shahi and Baker (2014) to extract strong-velocity pulses, following their extraction and selection criteria. However, because wavelet analysis cannot capture static offsets, which are another impact on pulse features, we developed a strategy to remove the static offsets from all recordings before the analysis of strong-velocity pulses. Before applying the static-offset correction to the signal, the signal was corrected for instrument drifts (Boore and Bommer, 2005) and preprocessed with Integrated Combined Baseline Modification (von Specht, 2019) to remove segmented instrument drifts and by the routine of Wang et al. (2011) to correct instrument drifts due to static-offset effects of the earthquake. In addition, in our processing, we assume that the amplitudes are component dependent with the same duration and can be represented by a hyperbolic tangential functional
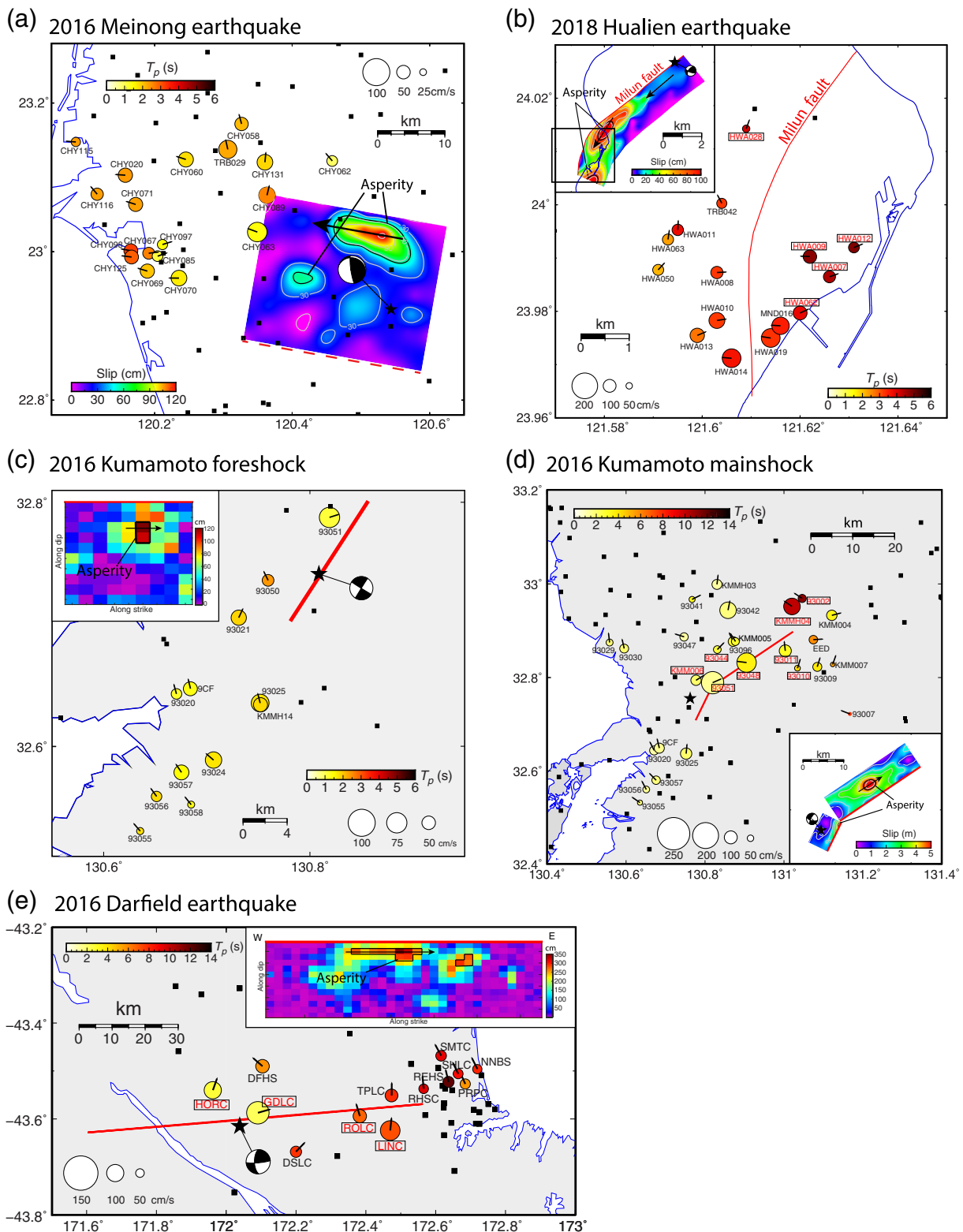
Figure 2. Distributions of strong-velocity pulses without the static-offset effect for: (a) the 2016 Meinong earthquake, (b) the 2018 Hualien earthquake, (c) the 2016 Kumamoto foreshock, (d) the 2016 Kumamoto mainshock, and (e) the 2010 Darfield earthquake. Circles represent the strong-velocity pulses identifiy in the events. The size of circles represent the amplitude of strong-velocity pulses. The color in circles represent the pules period, T_ρ. Arrows on the circles represent the orientation of the strongest pulses. The inset figure for each panel represents the slip distributions from the waveform inversion. The color in insets represent the slip distribution. The slip distributions of panels (a,b) are with respect to the inversion results of Lee *et al.* (2016; 2019), panel (c) is with respect to the inversion results of Kobayashi *et al.* (2017), panel (d) is with respect to the inversion results of Asano and Iwata (2016), and panel (e) is with respect to the inversion results of Hayes (NEIC, Darfield 2010). Arrows on the asperity represent the rupture direction within the asperity. Squares represent the station without pulses. The stations names with frame of which represent the pulses that are impacted upon the static offset. The color version of this figure is available only in the electronic edition.

form. The detailed theory and examples are provided in the supplemental material, available to this article.

After applying the static-offset corrections to all the records, we apply the wavelet analysis algorithm of Shahi and Baker (2014), which uses the wavelet transform of two horizontal orthogonal components of ground motion to search for orientations that are more likely to contain strong pulses. In this study, we use an order 4 Daubechies wavelet as the mother wavelet and define the strong-velocity pulse as the wavelet with the largest wavelet coefficient. The extracted pulse is a proxy of the signal associated with directivity and represents only the main features of the signal. The selected wavelet is then subtracted from the original ground motion to yield a residual ground motion, and the strength of a pulse is classified by the pulse indicator (PI; equation 1; Shahi and Baker, 2014):

$$PI = 9.384(0.76 - PC - 0.0616\ PGV)$$
$$(PC + 6.914 \times 10^{-4}PGV - 1.072) - 6.179, \qquad (1)$$

$$PC = 0.63 \times (PGV\ ratio) + 0.777 \times (energy\ ratio),$$

in which the principal component (PC) is the linear combination of two variables (peak ground velocity [PGV] ratio and energy ratio), the energy ratio is the energy ratio of residual and original ground motions, and the PGV ratio is the ratio of the residual and original PGV. The analyzed ground motion is labeled as a pulse if the PI value is positive and as a nonpulse if it is negative. This approach captures information about the pulse, such as its orientation, the associated PGV, and the value of the pulse period. It should be noted that the identified pulse period from this method should be considered as the apparent pulse period, because it depends on wavelet selection.

The static offset and directivity effects on strong-velocity pulse

Static offset and the rupture directivity effects are two physical phenomena resulting in large ground-motion pulses. Static offset is the result of elastic rebound theory, in which stress and strain energy are generated over a long time and suddenly released, causing a large permanent ground displacement (Bolt and Abrahamson, 2003). The result would be a long-period single-side velocity pulse, which is different from the directivity pulse (double slide) produced by the constructive interference of propagating seismic waves. The rupture directivity accompanied by the radiation pattern of the seismic source can indeed lead to constructive wave interference that appears in the form of a double-side velocity pulse (Somerville et al., 1997). The single-side and double-side velocity pulses can be clearly seen at stations 93002 for the 2016 Kumamoto mainshock and GDLC for the 2010 Darfield earthquake (Fig. 2). The pulse period might be the result of both static

offset and the directivity effects, if the earthquake is large enough with a strong directivity effect, such as the 2016 Kumamoto mainshock. Broadband simulations (Kamai et al., 2014) of the fling step (static offset) showed that the pulse periods associated with the fling effect increase with the strike-slip earthquake magnitude (**M** 6–8, periods between 1.8 and 10.8 s).

To analyze only pulses generated by wave interferences, we develop a strategy to separate the two phenomena from the observations. We perform the static-offset correction described in von Specht (2019) to all recordings to extract the static offset from those pulses. The permanent displacements estimated using the procedure by von Specht (2019) were already validated against Interferometric Synthetic Aperture Radar data. Figure 3 shows examples of the ground motions with and without the static-offset correction, extracted pulses resulting from the forward directivity and static-offset effects, and the static offsets for each event. The comparison of the waveforms before and after the static-offset corrections at stations with significant static offsets for the 2016 Kumamoto mainshock is shown in Figure A1. The differences in peak velocity and pulse periods of corrected and uncorrected ground motions are shown in Figure 4. For the 2016 Kumamoto mainshock, near-fault stations (rupture distance <8 km) with static offsets greater than 1 m show more than 20% difference either in the peak velocity or pulse period after the static-offset correction (93002 for the 2016 Kumamoto mainshock and GDLC for the 2010 Darfield earthquake). The static offsets show significant differences at some stations (93002 for the 2016 Kumamoto mainshock and GDLC for the 2010 Darfield earthquake). For the smaller earthquakes, the static offset has a lower impact on the velocity and period of the pulses. The differences in the pulse velocities and periods show that a significant static offset has a strong effect on velocity but a less clear correlation with the pulse period.

Comparison of the analyzed strong-velocity pulses with a global dataset

We compare our pulse periods extracted from recordings of the five moderate earthquakes after the static-offset removal to the 244 identified pulses from the Next Generation Attenuation-West2 database (Ancheta et al., 2013), previously published by Shahi and Baker (2014) and presented in Figure 1 and Table 2. These newly observed pulses are consistent with the empirical scaling relationships from previous studies. However, our dataset shows a weak dependency of the pulse periods on moment magnitude for the magnitude range between **M** 6 and 7.5. Our observations indicate that the within-event variability is large for each event. This large within-event variability and the fact that the earthquake magnitude is a poor indicator of the pulse period motivate the following analysis. It also re-affirms the necessity to perform the static-offset removal to investigate the effects of the strong-velocity pulse resulting from the forward rupture directivity.

Figure 3. Rotated ground motions along pulse orientations (thick curve) and extracted pulses (dashed curve) at stations CHY063 (2016 Meinong earthquake), HWA019 (2018 Hualien earthquake), 93051 (2016 Kumamoto foreshock), 93002 (2016 Kumamoto mainshock), and GDLC (2010 Darfield earthquake). Disp, displacement; Vel, velocity. The color version of this figure is available only in the electronic edition.
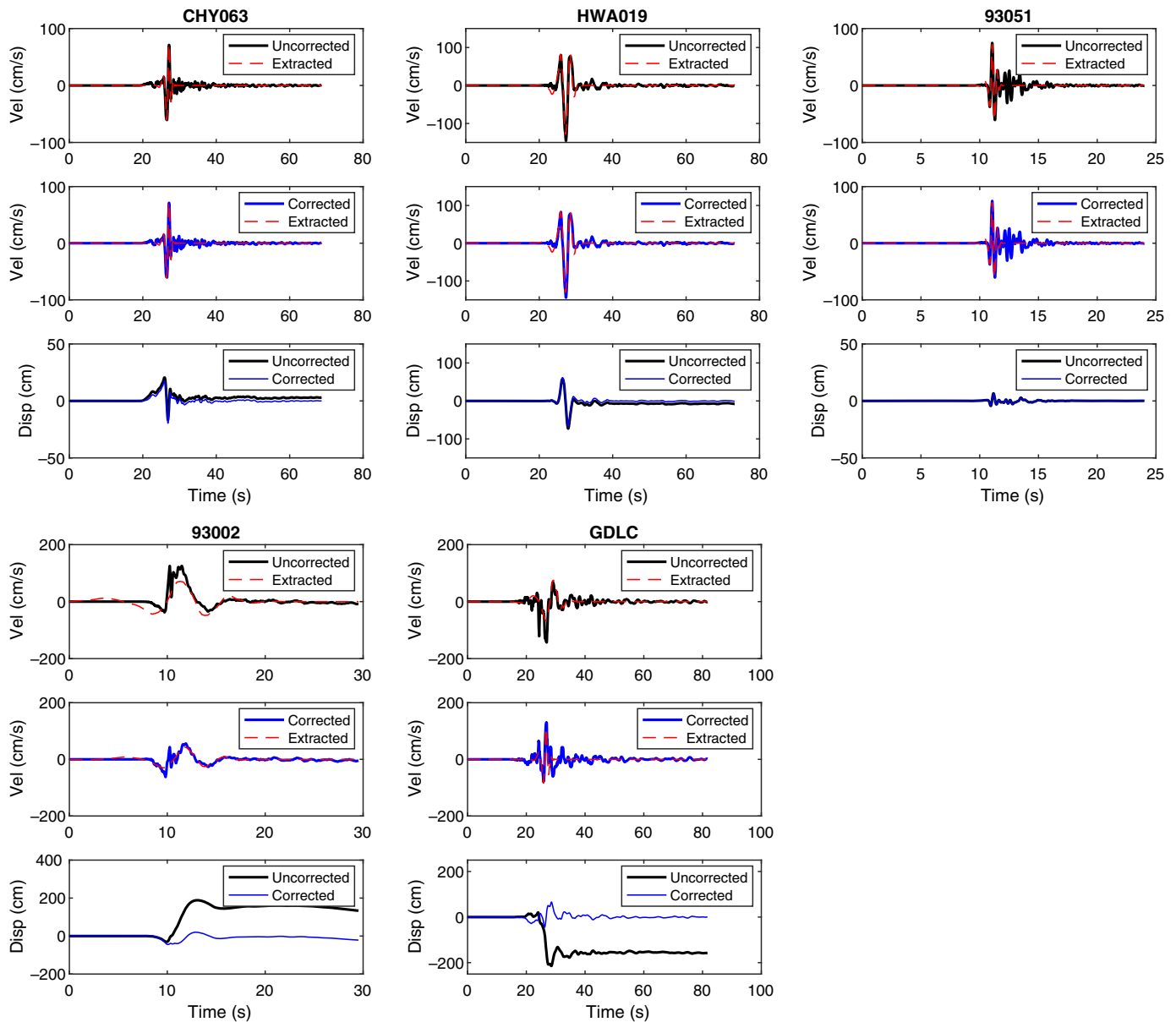
Figure 2 shows the distributions of the strong-velocity pulse periods after static-offset removal for the 2016 Meinong and 2018 Hualien earthquakes, the 2016 Kumamoto foreshock and mainshock, and the 2010 Darfield earthquake. The strong-velocity pulses generated by the 2016 Meinong earthquake are located in the westward rupture direction of the earthquake asperity at distances between 15 and 40 km (farthest station CHY115) from the asperity. The identified pulses show periods between 1 and 3 s. The identified pulses of the 2018 Hualien earthquake are also found along the rupture direction of a large asperity, but only in the near-fault area (rupture distance <3 km), with the pulse periods showing a large variability between 2 and 5 s. Compared to other similarly sized events (Fig. 1), the within-event variability of the pulse periods is considerably greater in the near-fault area of the 2018 Hualien earthquake. The identified pulses of the 2016 Kumamoto foreshock show periods between 1 and 2 s, with

the farthest station (93055) that identified such pulses being located at a rupture distance to the fault of 17 km. The identified pulses also show full-azimuthal coverage. We identified strong-velocity pulses for the Kumamoto mainshock up to 50 km from the rupture fault plane (farthest station: KMM001), with the identified pulses showing periods between 1 and 11 s. The within-event variability of the pulse periods is much larger for this large earthquake (M_w 7.04) compared to the variability observed for the aforementioned smaller events.
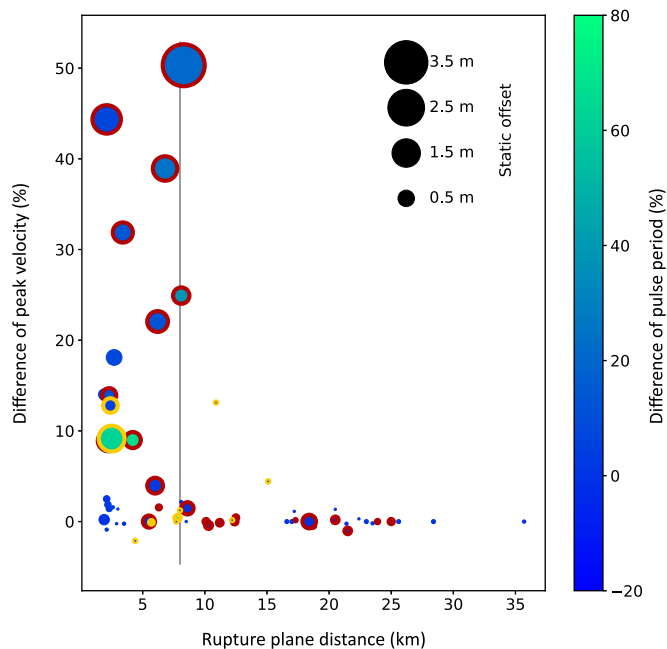
Figure 4. Comparison of pulse velocity and period before and after the static-offset removal. The color of the circle represents the difference of the pulse period with and without the static offset. The size of the circle represents the static offsets. Circles represent the pulses of the 2016 Kumamoto mainshock (dark outline) and the 2010 Darfield earthquake (light outline). The color version of this figure is available only in the electronic edition.

The identified pulses of the 2010 M_w 7.02 Darfield earthquake show pulse periods between 2 and 12 s.

We see strong pulses on the fault-normal (FN) component in the forward rupture direction from each event, but pulses at other near-fault stations are not only on the FN component. This observation may be due to the complexity of the slip distribution and near field and intermediate fields (the latter being not static) interfering with the forward directivity effect.

Dependency of pulse amplitude and periods on distances to the hypocenter and asperity

To discuss the dependency of pulse amplitude and periods with distance from the hypocenter and asperity, we first define the angle between a station and the striking direction of the fault at the hypocenter and the asperity, respectively. Figure 5a shows the geometrical setting for these definitions. The azimuth from the hypocenter (az_{hypo}) is the angle between the azimuth of the station and the rupture direction from the hypocenter. The azimuth from the asperity (az_{asp}) is the angle between the azimuth of the station and the rupture direction from the asperity. The azimuth from the asperity is calculated with respect to the center of the asperity. The asperity is that region on the fault plane slip of which is two times greater than the average slip over the entire fault plane, according to the definition of Somerville *et al.* (1999). We mark the asperities for all earthquakes in Figure 2.

We found that there is a decay in the peak velocity with increasing azimuth (absolute value) for the 2018 Hualien earthquake (Fig. 5b,c). The decay pattern spreads over a broader azimuth range and is thus more readily identifiable, considering the asperity azimuth (Fig. 5b) rather than the hypocenter azimuth (Fig. 5c).

The scaling of peak velocity and pulse period with the rupture plane distance is shown in Figure 6. Our newly identified pulses are consistent with the data (earthquakes with magnitudes between **M** 5.0 and 6.9) of Shahi and Baker (2014), with peak velocities decaying with increasing rupture plane distance. However, the scaling of the pulse period with rupture plane distance is not clearly correlated and shows a large variability (Fig. 6b). The additional records also show a large variability in the pulse properties at shorter rupture plane distances of large as well as moderate earthquakes.

STRONG-VELOCITY PULSES FROM SIMULATIONS
Simulation setting

To understand the factors driving the observed near-field pulse variability for moderate earthquakes, we performed simulations based on the $f\text{-}k$ approach (Zhu and Rivera, 2002). This method is adapted to the simulation and analysis of ground-motion pulses, because the static deformation can be obtained numerically using the dynamic solution at a near-zero frequency (Zhu and Rivera, 2002). The use of simple multilayered velocity models is also adapted to this study, because site effects play a minor role in pulse generation.

These simulations focus on the near-fault region of moderate earthquakes (rupture distance less than 15 km, Pacor *et al.*, 2018) in which the pulses have been mostly identified. The simulations' setting is based on those of the 2018 Hualien strike-slip earthquake, because most of the pulses are found for strike-slip earthquakes according to previous studies and our detected pulse cases. For the velocity structure, we consider the velocity model of Lin *et al.* (2020) for hard-rock site conditions near Hualien City (Table 3). Rupture initiation is set to occur at the northern vertical edge of the fault and propagates with a constant rupture velocity (2.4 km/s, 0.8 times the S-wave velocity) toward the south. The rupture extent is 7 km × 5 km for an event with a magnitude M_w 6.0. The focal depth of the 2018 Hualien earthquake was 6.3 km, and we set the focal depth as 5 km in the simulation, because additional simulations with M_w 6.0 but larger focal depth (10 km) showed that the velocity amplitudes are not high enough to be classified as a pulse for such greater depths. To analyze the impact of the asperity on pulse properties, we implement a basic asperity with a magnitude of M_w 5.8 in four cases (red stars in models IV–VII in Fig. 7). In these simulations, two cases are set for asperity location tests in which asperities are located at different distances from the hypocenter (the initial rupture point) with the lengths of 3.5 km (models IV and V), and the other two cases are set for asperity sizes tests in which the lengths of

Parameters Table of the Extracted Pulses

Earthquake Name	Year	Station Name	R_{rup} (km)	R_{hypo} (km)	T_p (s)	PGV (cm/s)	Orientation (w.r.t. North)
Kumamoto	2016	93002	8.3	37.7	11.2	62.2	−12
Kumamoto	2016	93009	10.3	33.4	4.3	70.4	18
Kumamoto	2016	93010	8.1	29.2	4.3	44.9	22
Kumamoto	2016	93011	3.4	28.1	3.1	93.4	−4
Kumamoto	2016	93020	12.5	19.6	1.2	69.3	−26
Kumamoto	2016	93025	8.6	18.1	2.0	87.6	5
Kumamoto	2016	93029	25.0	26.5	1.9	53.3	−7
Kumamoto	2016	93030	21.5	23.3	2.0	68.8	−11
Kumamoto	2016	93041	18.7	26.6	3.2	46.5	64
Kumamoto	2016	93042	12.5	25.9	1.8	126.8	11
Kumamoto	2016	93044	6.8	18.2	2.7	59.6	54
Kumamoto	2016	93048	2.1	20.1	3.6	150.1	82
Kumamoto	2016	93051	2.2	14.0	1.5	172.0	67
Kumamoto	2016	93055	23.9	30.3	1.8	40.2	−55
Kumamoto	2016	93056	20.5	27.2	1.4	52.4	−27
Kumamoto	2016	93057	17.3	24.5	1.8	65.5	−44
Kumamoto	2016	93096	6.3	21.0	3.1	75.6	−20
Kumamoto	2016	9CF	11.2	18.7	1.6	78.3	−13
Kumamoto	2016	EED	5.5	34.6	5.8	65.8	86
Kumamoto	2016	KMM004	10.1	40.9	4.0	81.2	−42
Kumamoto	2016	KMM005	6.0	21.2	2.9	60.6	−46
Kumamoto	2016	KMM006	4.2	13.2	2.0	80.0	57
Kumamoto	2016	KMM007	12.4	36.9	5.5	34.5	19
Kumamoto	2016	KMMH03	18.4	30.4	1.3	76.8	7
Kumamoto	2016	KMMH04	6.2	34.8	10.1	127.9	−42
Meinong	2016	CHY020	28.4	46.6	2.4	51.0	−86
Meinong	2016	CHY058	23.6	38.3	2.1	53.2	−15
Meinong	2016	CHY060	24.0	40.6	1.8	57.6	−72
Meinong	2016	CHY062	21.6	28.2	0.9	40.1	−40
Meinong	2016	CHY063	16.6	27.8	1.4	71.2	−69
Meinong	2016	CHY067	21.4	40.1	2.6	42.8	83
Meinong	2016	CHY069	20.5	39.9	2.0	51.2	−73
Meinong	2016	CHY070	17.0	35.6	1.7	58.6	−90
Meinong	2016	CHY071	25.6	43.8	2.3	50.5	−72
Meinong	2016	CHY085	20.4	38.9	1.1	39.8	71
Meinong	2016	CHY089	18.9	29.4	2.6	61.8	13
Meinong	2016	CHY097	20.6	38.6	1.5	37.7	73
Meinong	2016	CHY098	23.5	42.6	3.2	51.1	−79
Meinong	2016	CHY115	35.7	55.0	2.3	34.5	−85
Meinong	2016	CHY116	30.4	49.3	2.4	45.5	−40
Meinong	2016	CHY125	23.0	42.3	2.9	51.4	−83
Meinong	2016	CHY131	20.9	32.5	1.9	57.8	6
Meinong	2016	TRB029	22.4	37.1	2.3	66.5	−12
Hualien	2018	HWA007	2.3	19.6	4.0	80.9	83
Hualien	2018	HWA008	2.1	20.0	3.3	93.7	−88
Hualien	2018	HWA009	2.2	19.3	4.1	96.3	−78
Hualien	2018	HWA010	2.1	20.9	3.3	125.1	82
Hualien	2018	HWA011	3.0	19.6	3.8	88.0	4
Hualien	2018	HWA012	2.7	19.0	4.5	68.8	81
Hualien	2018	HWA013	2.3	21.2	2.7	110.6	66
Hualien	2018	HWA014	2.2	21.4	3.6	142.8	−84
Hualien	2018	HWA019	1.9	20.9	3.3	144.1	−73
Hualien	2018	HWA028	2.6	28.0	4.0	56.4	23
Hualien	2018	HWA050	2.9	20.3	2.3	85.8	35
Hualien	2018	HWA062	1.9	20.6	3.6	93.3	74
Hualien	2018	HWA063	3.0	18.9	2.3	85.6	8

(*continued*)

TABLE 2 (*Continued*)

Earthquake Name	Year	Station Name	R_{rup} (km)	R_{hypo} (km)	T_p (s)	PGV (cm/s)	Orientation (w.r.t. North)
Hualien	2018	TRB042	2.8	16.9	3.2	72.5	−30
Darfield	2010	DSLC	8.5	17.9	7.8	65.6	44
Darfield	2010	GDLC	2.5	12.0	2.3	141.0	74
Darfield	2010	HORC	7.8	15.0	2.7	99.5	19
Darfield	2010	LINC	5.7	36.3	7.2	114.5	6
Darfield	2010	NNBS	15.1	57.5	10.7	54.6	−27
Darfield	2010	REHS	8.0	50.4	12.0	256.2	−13
Darfield	2010	RHSC	4.2	44.6	9.4	64.0	−6
Darfield	2010	ROLC	2.4	29.8	6.9	82.2	−17
Darfield	2010	SHLC	10.9	53.0	8.4	62.3	−26
Darfield	2010	SMTC	12.2	50.4	9.2	61.8	−28
Darfield	2010	TPLC	3.4	37.3	7.9	74.8	0
KumaFore	2016	KMMH14	1.9	9.7	1.8	52.3	−12
KumaFore	2016	93020	7.7	13.2	1.3	39.0	−15
KumaFore	2016	93021	4.4	7.3	1.8	57.8	25
KumaFore	2016	93024	8.1	15.2	1.7	59.0	−49
KumaFore	2016	93025	1.8	9.6	1.7	64.5	−14
KumaFore	2016	93050	3.5	7.3	2.5	43.2	−26
KumaFore	2016	93051	4.6	12.1	1.2	74.6	72
KumaFore	2016	93055	17.2	23.8	1.8	26.3	−40
KumaFore	2016	93056	13.9	20.5	1.8	37.6	−36
KumaFore	2016	93057	10.7	17.5	1.5	54.3	−34
KumaFore	2016	93058	12.6	19.5	1.4	25.5	−38
KumaFore	2016	9CF	6.4	12.0	1.4	51.3	−14

R_{hypo}, distance to the hypocenter; R_{rup}, distance to the rupture plane; Orientation (w.r.t. north), orientation of the strongest observed pulse, in degrees clockwise from north; PGV, peak ground velocity of the strongest observed pulse; and T_p, the period of the extracted pulse in the direction of the strongest observed pulse.

asperities are equal to 2.1 and 4.9 km (models VI and VII). Because strong-velocity pulses are found in earthquakes with different mechanisms, we also tested the impact of various fault dip angles (90°, 70°, and 50° dipping to east, models I–III) with homogeneous slip distributions, giving in total seven fault models (models I–VII in Fig. 7). Several observation points are set along and near the fault to investigate the pulse characteristics at these locations (Fig. 7).

Pulse detection and probabilities

Examples of synthetic ground-motions and identified pulses (homogeneous slip and heterogeneous slip with asperities near and far from the hypocenter) are shown in Figure 8. The identified pulses are readily extracted from the synthetic waveforms in the near-fault region (stations 007–m04), and the PI (equation 1) is high for these waveforms, indicating a clear strong-velocity pulse. The resulting PI is less than 10 when the waveforms contain multiple phases, and waveforms with PI < 10 are considered to not be representative of strong-velocity pulses. Figure 9 shows the spatial distribution of PIs for cases with heterogeneous slip and asperities. The figure shows that the PI pattern is dominated by the asperity locations. Pulse amplitudes noticeably increase in the vicinity of the asperities in the forward rupture direction with generally higher PIs closer to the asperity. The effect increases with increasing distance of the asperity from the hypocenter, highlighting the significant

effect of the asperities on strong-velocity pulses. In Figure 9, we show the probability of observing a pulse according to Shahi and Baker (2014, equation 23). The highest pulse probability in these cases is around 0.5 and decays approximately radially. The pulse distributions from the simulations show that most of the pulses are concentrated near the fault, especially near the asperity, and the occurrence of the pulses decays quickly with the rupture plane distance. The comparison between the probabilistic model of Shahi and Baker (2014) and our simulations implies a model overestimation of the occurrence of pulses at moderate distances (greater than 10 km). The empirical Shahi and Baker (2014) model was calibrated from a database, including mainly large earthquakes (M >6.5), and our findings suggest that their relationship cannot be extrapolated to smaller, moderate-sized events.

Impact of asperity properties on pulse characteristics

Figure 10 displays the distribution of the pulses extracted from simulations performed with various asperity locations and sizes. The simulations confirm the large within-event variability of the pulse periods. The pulse periods in all cases are short for the stations in the forward rupture direction, as expected from the directivity effect. The ranges of pulse periods are similar for the cases with homogeneous and heterogeneous slip, whereas the asperities control the pulse periods and spatial distribution with pulse periods being shorter at stations near the asperity.
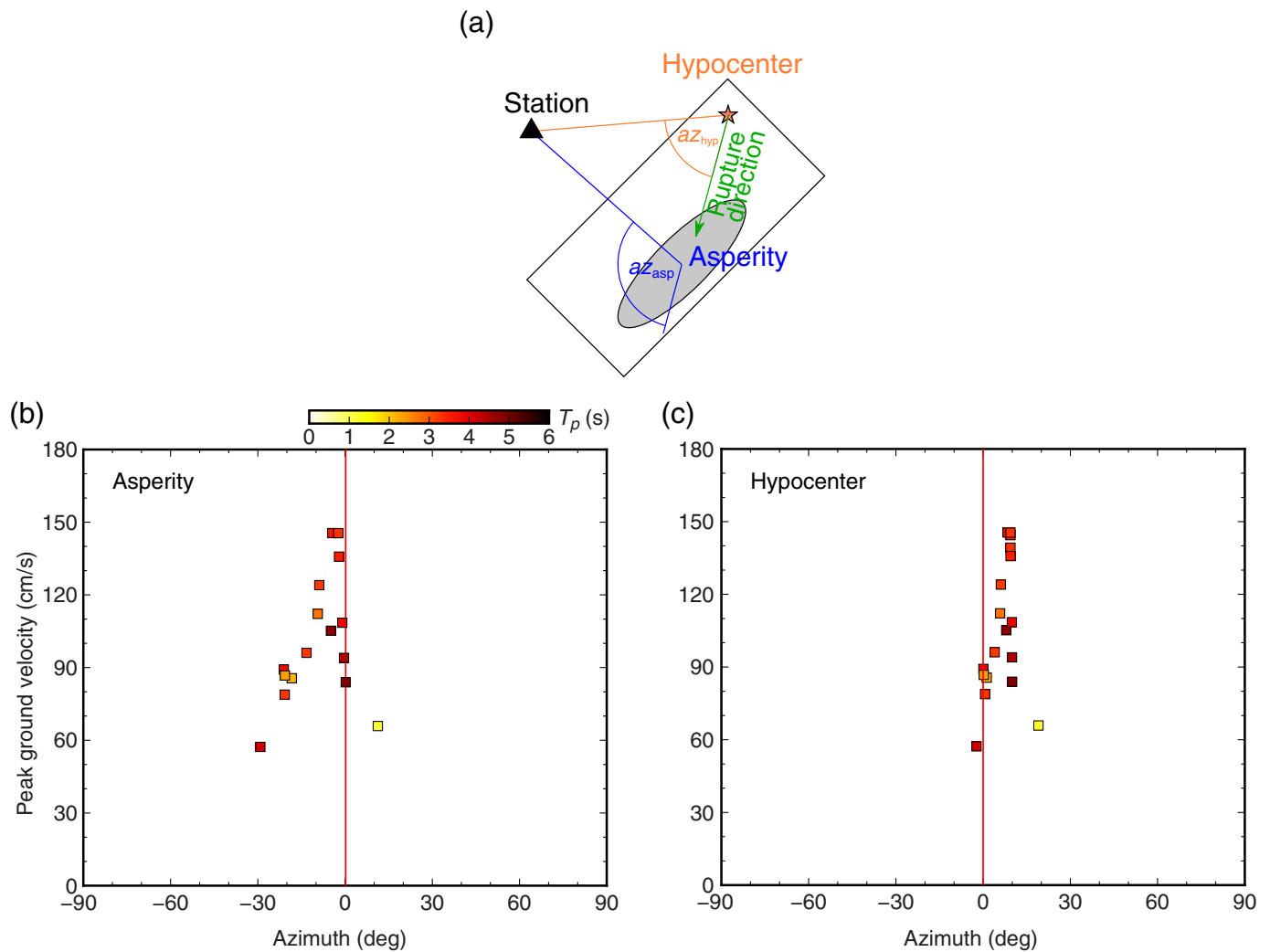
(a)

(b) **(c)**

Figure 5. (a) Geometrical setting for the definitions of the azimuth from the hypocenter (az_{hypo}) and the azimuth from the asperity (az_{asp}). Peak ground velocity (PGV) as a function of the angle between the rupture direction (b) from the asperity and (c) from the hypocenter and stations' azimuth for the 2018 Hualien earthquake. Azimuth indicates the angle between the station's azimuth to the rupture direction within the asperity. The color version of this figure is available only in the electronic edition.

The asperity properties also control the ground-motion velocity amplitudes. The spatial distribution of high-pulse velocities is controlled by the asperity location, and the pulse velocity is higher at stations located near the asperity. Asperities with a small dimension and a higher slip would increase the ground-motion velocity amplitudes. The ground motions near the asperity contain stronger phases and higher PI (Figs. 9 and 10). If the asperity is located far from the hypocenter, pulse velocities within a few fault lengths from the rupture are higher than in those cases in which the asperity is located near the hypocenter (Fig. 8, models IV and V; Fig. 10b,c).

Impact of dipping angles on pulses characteristics

Pulse velocities as a function of the azimuth between the rupture direction and the stations for various dipping angles are shown in Figure 11. The pulse velocities at stations in the rupture direction (red lines in Fig. 11) are higher and decay with increasing absolute azimuth. For a shallow-dipping fault, the velocities on the hanging wall are higher than those on the footwall, and the pulses with high velocities are distributed over an extended area compared to the vertical-fault case. When the dip approaches 90°, the velocity decay pattern

becomes symmetrical, and the high velocities are focused near the fault. Ground-motion velocities generated by the 2018 Hualien event are large, and the decay pattern is much clearer than those observed from the other studied earthquakes. The results from both simulations and observations confirm that the fault-dipping angle affects the pulse velocity amplitude and its spatial distribution. The directivity effect of a vertical strike-slip fault is large, which increases the pulse velocity recorded at stations located along the rupture plane azimuth.

If the station is in the rupture direction (azimuth = 0°) and for subshear rupture velocities, the direction of wave propagations is concentrated, the strong phases gather within a narrow time band, and the periods become shorter. This effect,
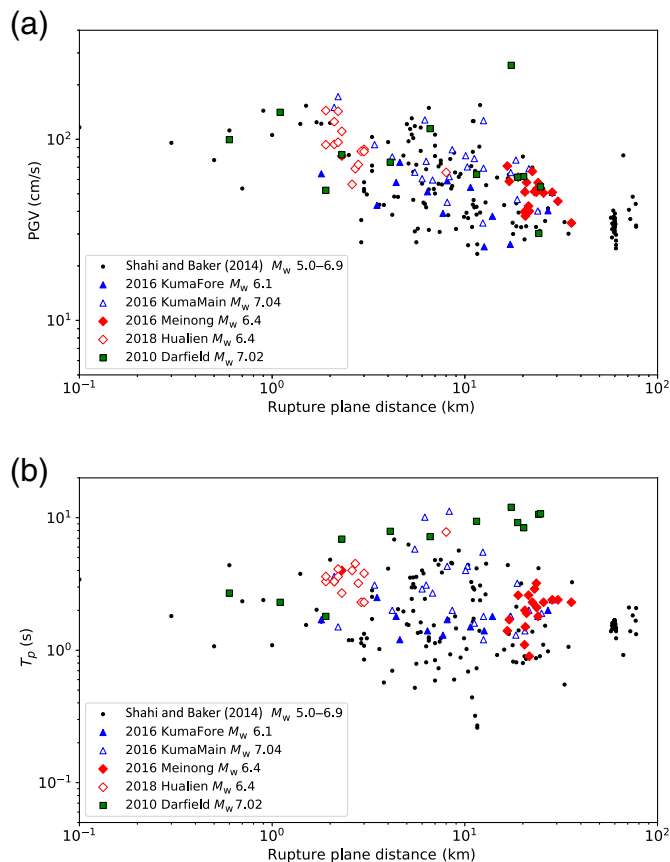
Figure 6. Scaling of (a) PGV and (b) pulse period, T_p, according to the rupture plane distance. The data of Shahi and Baker (2014) are shown for earthquakes magnitudes between 5.0 and 6.9. The static offset of the events has been removed. The color version of this figure is available only in the electronic edition.

produced by the asperity, is only found within shorter distances of around 6 km from the asperity and along the rupture direction for the case of an M_w 6.0 event with an M_w 5.8 asperity.

DISCUSSION

Several studies have proposed empirical regression relationships between pulse periods and earthquake magnitudes (Somerville, 2003; Shahi and Baker, 2011, 2014). Our updated database of pulses produced by the directivity effect indicates a weak dependency of pulse periods on earthquake moment magnitude within the range **M** 6–7.5 (Fig. 1). We confirm a large within- and between-event variability in the pulse periods, although also showing that the occurrence probability of strong-velocity pulses for moderate earthquakes (**M** <6.5) decreases quickly with rupture distance (compared to the decayed pattern from the empirical model of Shahi and Baker, 2014).

Our analysis shows that pulses in the near field are controlled by source characteristics such as rupture direction,

rupture distance, and asperity properties. Figure 11 compares pulse velocities and periods with respect to asperity properties at near-fault stations shown in Figure 7. The pulse periods are sensitive to the azimuth between rupture direction and station, and are shorter at the stations in the rupture direction and increase with the angle between the rupture direction to the stations (for a subshear rupture velocity). The pulse velocity amplitudes are observed to be controlled by the asperity locations and sizes, in which the presence of the asperity increases the ground-motion velocity amplitude significantly at stations near it. Velocity amplitudes are higher if the asperity is located far from the hypocenter or if the asperity is characterized by a higher slip within a smaller patch, even though the total magnitudes of the slips are identical. Pulse characteristics are considerably variable in the near field for earthquakes with different asperity properties, even with the same magnitudes.
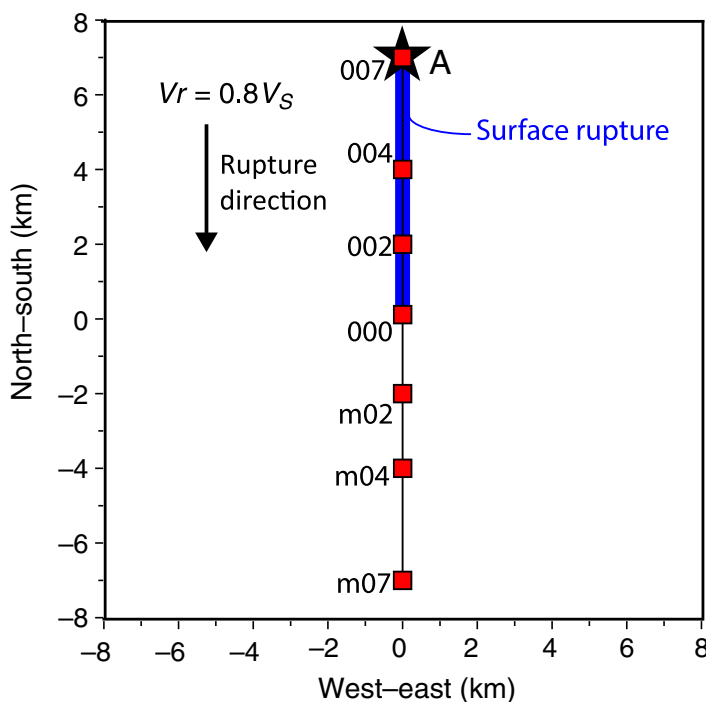
We further quantify the within-event variability of the pulse periods from simulations and observations, and compare these observations to the theoretical period predicted by Shahi and Baker (2014, equation 2), in which T_p is the pulse period, and M is moment magnitude:

$$\ln T_p = -6.55 + 1.12M. \qquad (2)$$

Figure 12a,b displays the comparison of the mean and standard deviation of the pulse periods from observations, simulations, and the predicted periods from the empirical equation (Shahi and Baker, 2014). The observed mean values show large between-event variations but remain within two standard deviations (95% confidence interval) of the empirical equation. For example, the 2016 Meinong and 2018 Hualien events are characterized by the same magnitude but show different mean values of T_p. This reflects how the effect of static offsets on the pulse period variability is not consistent from one earthquake to another; for the 2018 Hualien event, the variability in T_p decreases after the static-offset correction, but for the 2010 Darfield event, an opposite effect is found, and the variability in T_p increases after the static-offset correction is applied.

Nonetheless, the within-event variabilities of these moderate earthquakes are less than the variability from the Shahi and Baker (2014) regression. This lower observed variability from the considered observations is expected, because the variability of their regression represents the combined effect of the within- and between-event variabilities. The within-event variabilities of large earthquakes (2016 Kumamoto mainshock and 2010 Darfield earthquake) are larger than the variabilities of smaller events. This suggests that within-event variability may be magnitude dependent and be greater for larger earthquakes.

Kamai et al. (2014) evaluated the mean and standard deviation of the period and amplitude of the fling step from observations and simulations. The comparison of their model to our results is shown in Figure A2. The mean period
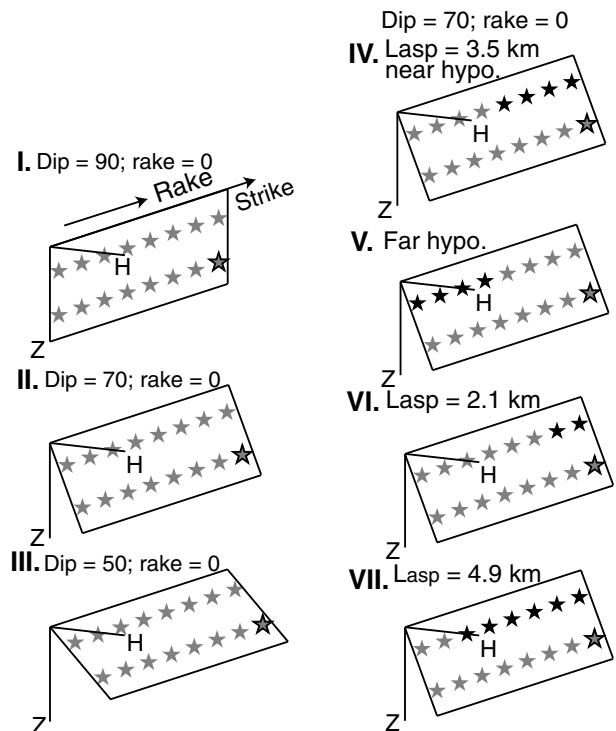
Figure 7. Simulation setting. The rupture velocity (V_r) is set at 2.4 km/s (0.8 times the S-wave velocity [V_S], 3.0 km/s). Squares represent the stations (007–m07) for the comparison in Figure 8. The star in map view and stars with outlines in the fault view indicate the initial rupture point. The right panel shows the fault geometry models. In each case, black stars are asperities (the total magnitude of the asperity is M_w 5.8 for each case). Gray stars are the subevents with background slips. The color version of this figure is available only in the electronic edition.

in our study is consistent with the 90% confidence interval of their model. We take the 2016 M_w 7.04 Kumamoto mainshock, from which we identified several pulses with significant static offset as an example. The fling-step pulse period for an M_w 7.02 event is 5.5 s, and the distance-dependent standard deviations lie between 0.58 and 0.92 s, according to the study of Kamai *et al.* (2014). In our analysis of the 2016 Kumamoto mainshock, the mean pulse period (with the static offset) is 5.2 s, and the standard deviation is 0.69 s (Fig. 12).

We further compare the pulse periods arising within the rupture distance of 15 km from real events and simulations (Fig. 12c). In the near-fault region, the mean pulse periods from observations and simulations are within two standard deviations (95% confidence interval) of the empirical equation of Shahi and Baker (2014) but show large between-event variability and higher values. The mean periods from seven simulation cases and their within-event variabilities are similar to each other; however, the spatial distributions of the pulses (Fig. 10) are quite different and depend on the properties of the asperity. Dense distribution of datasets then confirms the importance of the within-event variability that can be reproduced by the simulations. Pulse characteristics in the near-field show a strong relationship with nearby and local slip heterogeneities and variable rupture velocities on the fault planes (Figs. 10 and A3), in which such large within-event variability is significant, even for moderate earthquakes. This suggests that pulse periods are not only magnitude dependent, but that the rupture distance and heterogeneities on the fault plane should be considered.

This study also shows that the quantitative classification and identification of pulses are of considerable importance
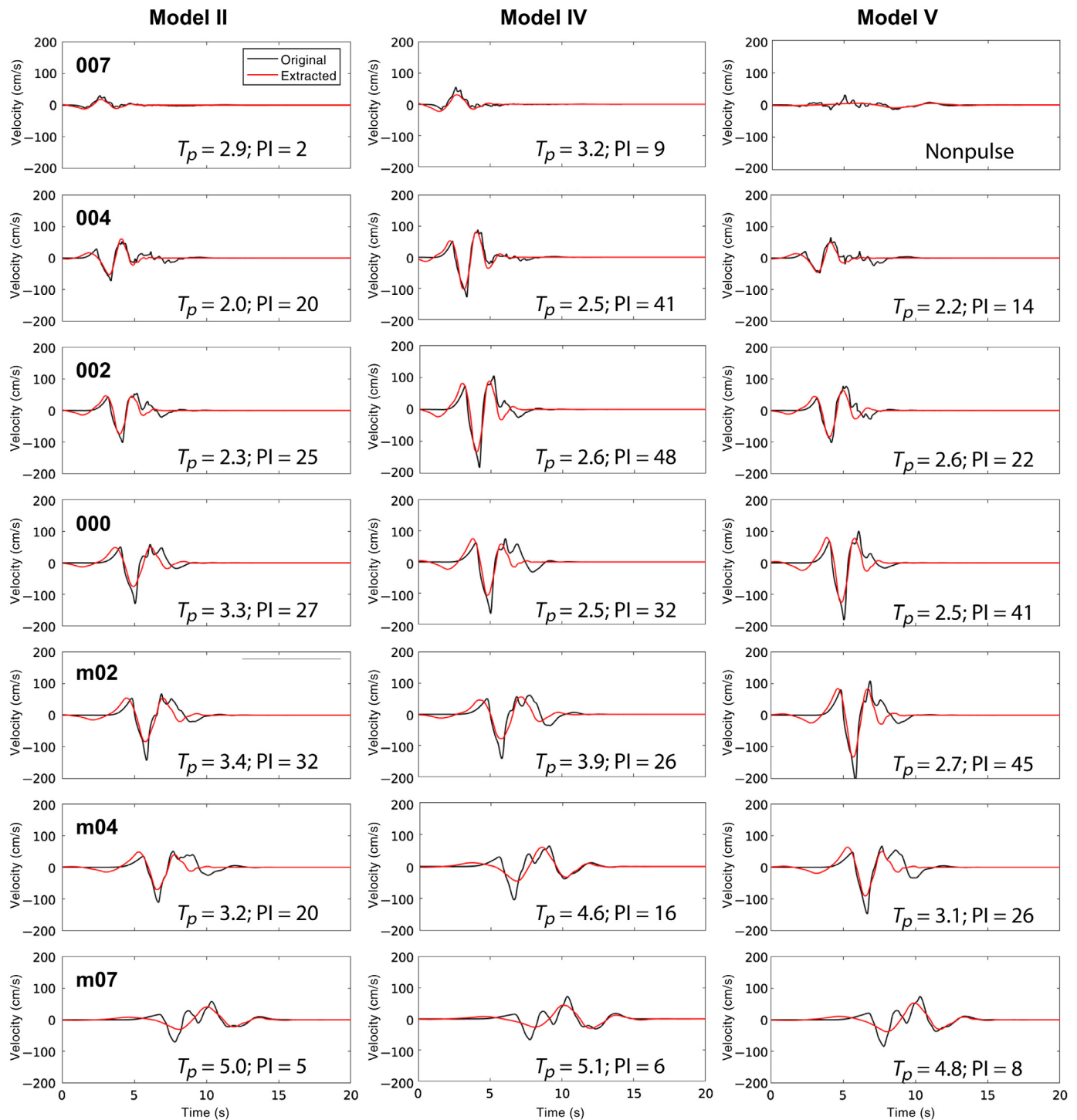
TABLE 3
1D Velocity Structure Used in the Simulations

Thickness (km)	V_P (km/s)	V_S (km/s)	Density (g/cm³)	Q_P	Q_S
0.5	3.57	2.09	2.6	600	300
2.5	4.21	2.55	2.6	600	300
3.0	4.89	2.95	2.6	600	300
4.0	5.58	3.24	2.6	600	300
5.0	5.87	3.41	2.6	600	300
5.0	6.14	3.56	2.6	600	300
5.0	6.44	3.70	2.6	600	300
5.0	6.71	3.82	2.6	600	300
5.0	6.96	3.97	2.6	600	300
5.0	7.19	4.12	2.6	600	300
5.0	7.45	4.24	2.6	600	300
5.0	7.63	4.32	2.6	600	300
5.0	7.78	4.42	2.6	600	300

This model refers to the velocity structure near Hualien City for hard-rock site conditions (Lin *et al.*, 2020).

Figure 8. Examples of the simulated ground motions (dark curves) and extracted pulses (light curves). The pulse indicator (PI) indicates the reliability level of the extracted pulses. The locations of the stations are shown in Figure 7. The color version of this figure is available only in the electronic edition.
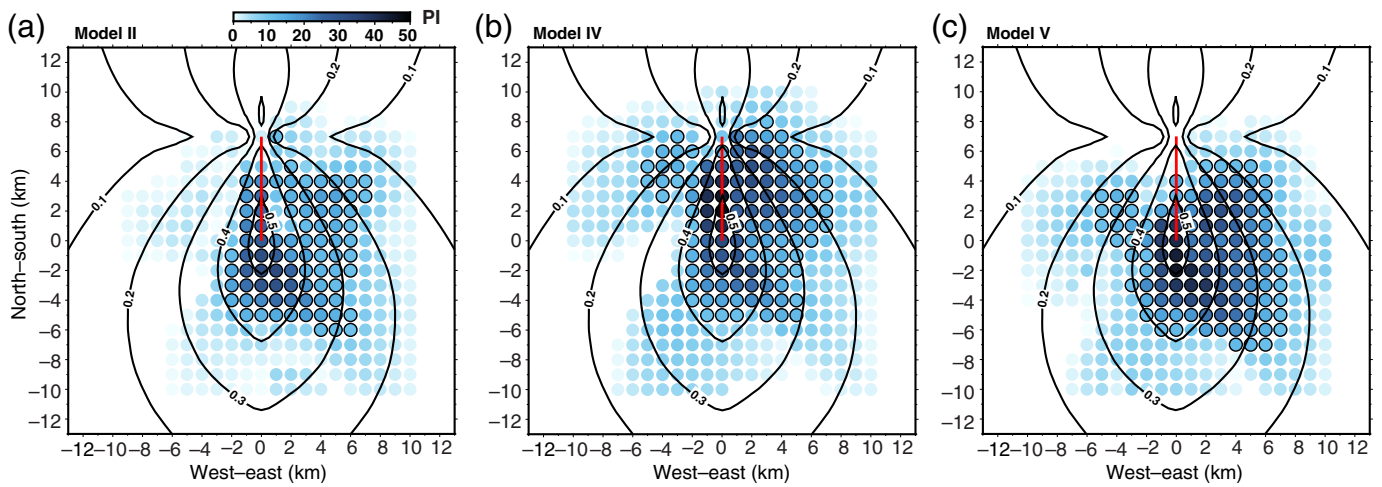
to investigate more accurately and efficiently the characteristics of ground-motion pulses. We have used the method developed by Shahi and Baker (2014), which can identify pulses at arbitrary orientations from multicomponent ground motions with low computational effort. However, the method has some shortcomings in that the pulses extracted are based on particular wavelets. Pulses with multiple phases cannot be extracted using this method, and the current method may overestimate the period of smooth peaks.

Figure 9. PI distribution of simulations for the considered asperities cases: (a) the homogenous slip (model II shown in Fig. 7), (b) case with the asperity near the hypocenter (model IV shown in Fig. 7), and (c) case with the asperity far from the hypocenter (model V shown in Fig. 7). The contours indicate the probability of pulses (Shahi and Baker, 2014, equation 23). Circles indicate the pulses from the simulations. The color shows the PI values. The circles with outlines represent the pulses with PI > 10. The color version of this figure is available only in the electronic edition.
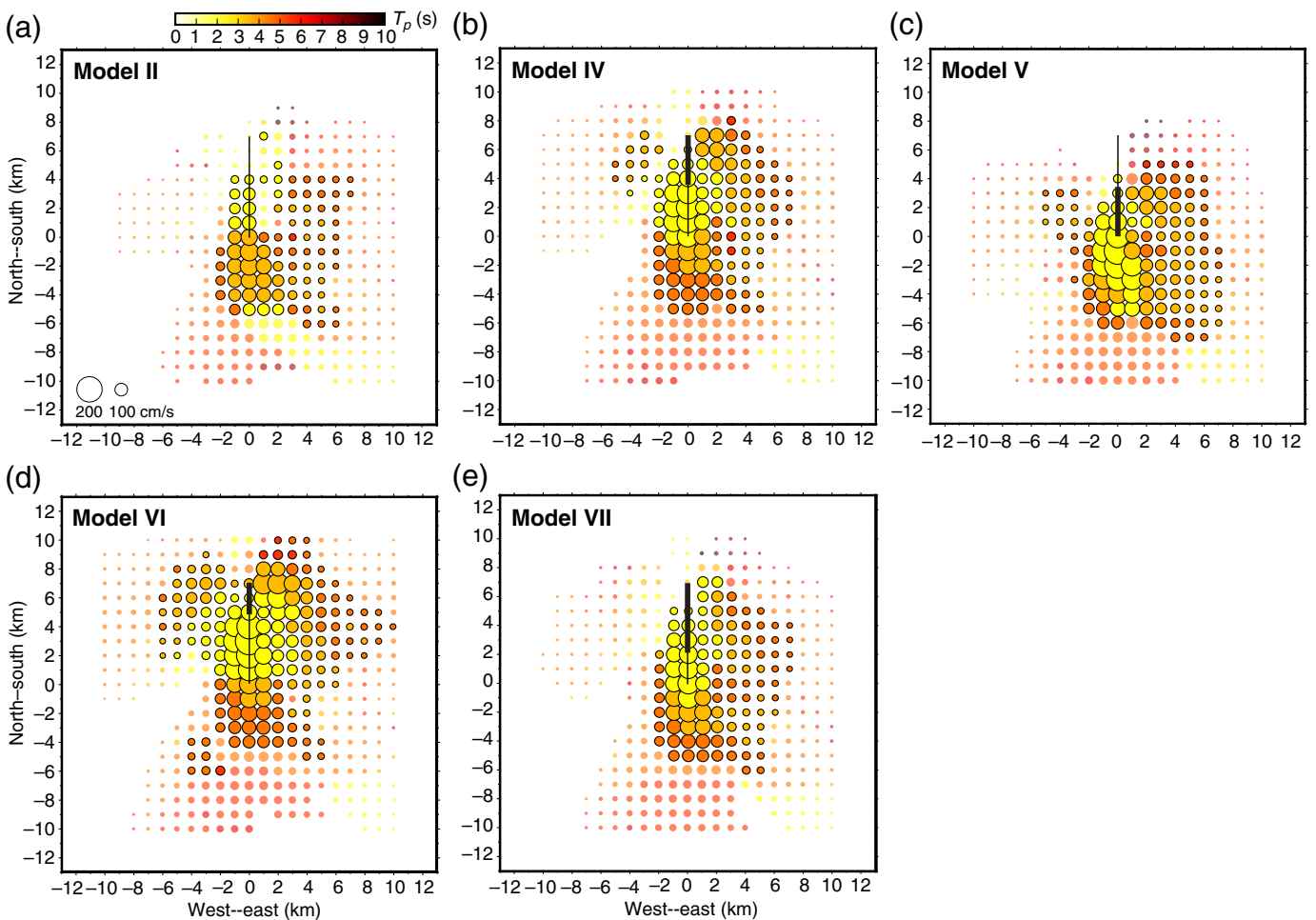
Figure 10. Distribution of the pulses for various asperity locations and sizes. The circle color represents the pulse period, and the size of the circle represents the pulse velocity. Circles with outlines represent the pulses with PI > 10. The settings of (a) model II, (b) model IV, (c) model V, (d) model VI, and (e) model VII are shown in Figure 7. The color version of this figure is available only in the electronic edition.

Figure 11. Pulse velocities as a function of azimuth, which is defined in Figure 5 for various dipping angle cases: (a) 50° dipping to east, (b) 70° dipping to east, (c) 90°, (d) the 2016 Meinong earthquake with a 22° dipping fault, (e) the 2018 Hualien earthquake with a 67° dipping fault, (f) the 2016 Kumamoto mainshock with a 72° dipping fault, (g) the 2016 Kumamoto foreshock with an 89° dipping fault, and (h) the 2010 Darfield earthquake with an 82° dipping fault. The static offset has been removed. The color version of this figure is available only in the electronic edition.

CONCLUSIONS

This study focuses on the strong-velocity pulse produced by the forward directivity effect from moderate earthquakes. Such events happen more frequently than large earthquakes and as such require attention in terms of seismic hazard assessment because of their damaging potential. We analyzed recent observations and performed simulations to understand the physical factors driving the variability of strong-velocity pulses. Ground-motion pulses are controlled by two main physical phenomena: the static offset and forward directivity effects. We developed a strategy to remove the static-offset effect from the observed ground motions. The results show that the static offset affected the pulse characteristics of large magnitude events for near-fault stations. The significant static offset has a strong effect on velocity amplitude, but it has a less clear correlation with the pulse period. Most of the records still show

a pulse behavior after the static-offset correction. This confirms that the identified pulses are mainly resulting from wave propagation and interferences.

The comparison of our observations and simulations with a model classically used in engineering seismology (Shahi and Baker, 2014) suggests that this model may overestimate the occurrence of pulses at moderate distances (>10 km) for
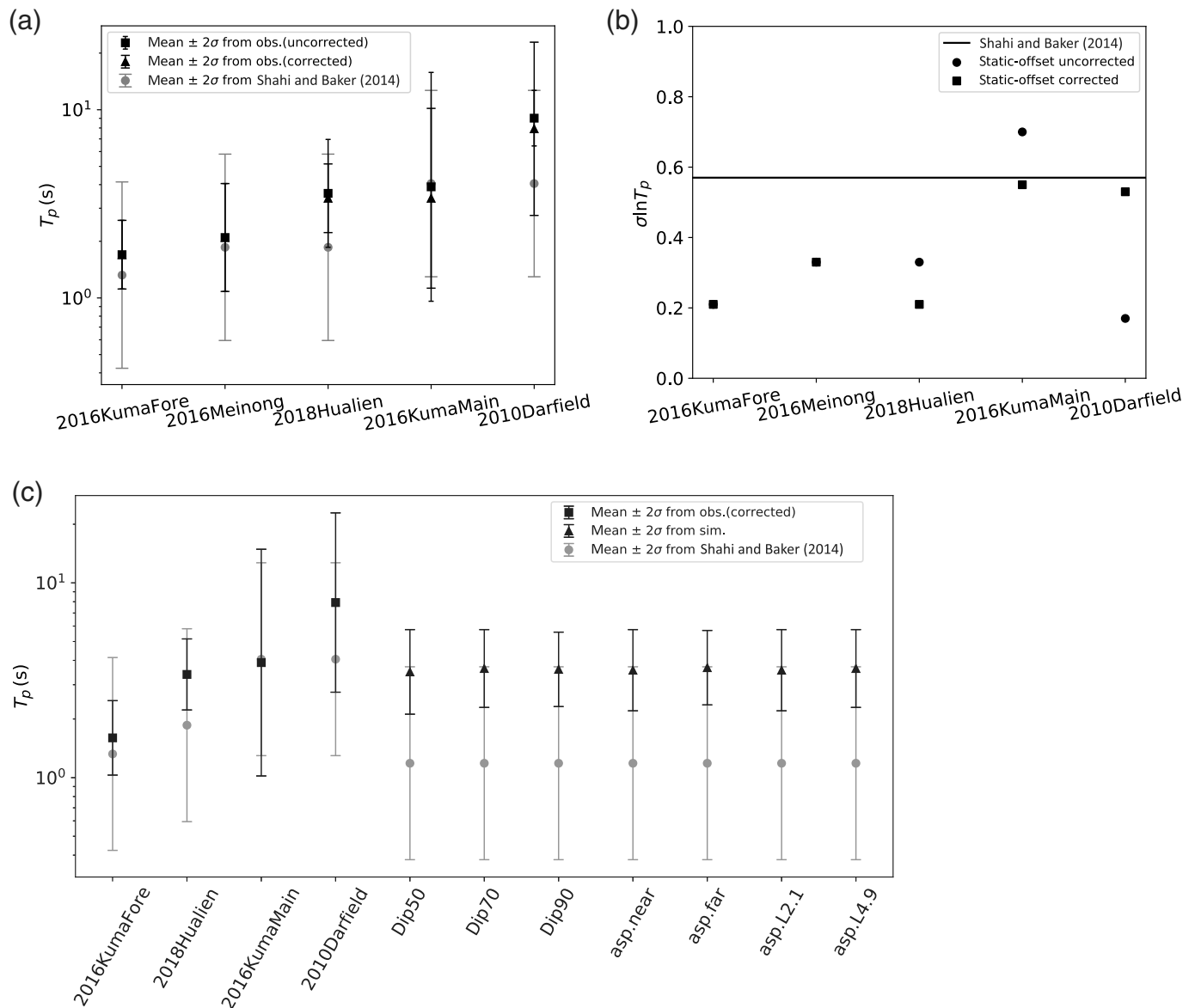
moderate strike-slip earthquakes, and that the variability of classical empirical relationships is largely controlled by the within-event variability. The within-event variability of pulse periods shown in our newly identified pulses indicates a dependency on magnitude.

The findings presented in this work reveal that the pulse velocity amplitude is sensitive to the asperity locations and sizes, in which the pulse velocity amplitude and the pulse period are controlled by the distance to the asperity, the azimuth between rupture direction of the asperity and station, and slip and rupture velocity heterogeneity on the fault.

As a long-term goal, a better understanding of the physical factors controlling the locations and properties of earthquakes asperities is necessary to predict future pulse properties. For a short-term goal, the potential controlling factors (e.g., the style of faulting) of within-event variabilities should also be investigated. Finally, engineering applications need to consider these potentially large within-event variabilities of the pulse

Figure 12. (a) Comparison of the observed (obs.) mean pulse periods from all pulses in the events and the mean periods calculated from the equation of Shahi and Baker (2014, equation 21). (b) Standard deviation of $\ln Tp$ corresponding to the events in panel (a). The line represents the standard deviation from the empirical regression (Shahi and Baker, 2014, equation 21). Circles represent the standard deviation before removing static offsets. Squares represent the standard deviation after removing static offsets. (c) Comparison of the observed (obs.) and simulated (sim.) mean pulses periods within a rupture distance of 15 km and the periods calculated from the equation of Shahi and Baker (2014, equation 21).

properties to more accurately carry out seismic hazard assessments.

DATA AND RESOURCES

The waveform data of 2016 Meinong and 2018 Hualien earthquakes were provided by the Taiwan Strong Motion Instrumentation Program (TSMIP) network of the Central Weather Bureau of

Taiwan and downloaded from the database of near-fault strong motions with pulse-like velocity in Taiwan (http://nfpv.ncree.org.tw/). The waveform data of 2016 Kumamoto foreshock and mainshock were provided by the K-Net and KiK-Net strong-motion networks (https://www.kyoshin.bosai.go.jp) of the National Research Institute for Earth Science and Disaster Resilience, and the strong-motion network of the Japanese Meteorological Agency. The waveform data of the 2010 Darfield earthquake were provided by the GNS strong-motion networks at https://static.geonet.org.nz/info/resources/applications_data/earthquake/strong_motion/ForStructuralAnalyses.zip. The method for the static-offset removal and its detailed theoretical account is provided in the supplemental material. An open-source MATLAB implementation of the proposed pulse classification algorithm which published by Shahi and Baker (2014) is available at http://github.com/shreyshahi/PulseClassification. All websites were last accessed in May 2021.

ACKNOWLEDGMENTS

REFERENCES

Almufti, I., R. Motamed, D. N. Grant, and M. Willford (2015). Incorporation of velocity pulses in design ground motions for response history analysis using a probabilistic framework, *Earthq. Spectra* **31,** no. 3, 1647–1666, doi: 10.1193/032113EQS072M.

Ancheta, T., R. Darragh, J. Stewart, E. Seyhan, W. Silva, B. Chiou, K. Wooddell, R. Graves, A. Kottke, D. Boore, *et al.* (2013). PEER NGA-West2 database, *Technical Report 2013/03*, Pacific Earthquake Engineering Research Center, Berkeley, California.

Asano, K., and T. Iwata (2016). Source rupture processes of the foreshock and mainshock in the 2016 Kumamoto earthquake sequence estimated from the kinematic waveform inversion of strong motion data, *Earth Planets Space* **68,** 147, doi: 10.1186/s40623-016-0519-9.

Baltzopoulos, G., L. Luzi, and I. Iervolino (2020). Analysis of near-source ground motion from the 2019 Ridgecrest earthquake sequence, *Bull. Seismol. Soc. Am.* **110,** no. 4, 1495–1505.

Bolt, B., and N. Abrahamson (2003). Estimation of strong seismic ground motion, in *International Handbook of Earthquake and Engineering Seismology*, Vol. 81B, Academic Press, 983–1001.

Boore, D. M., and J. J. Bommer (2005). Processing of strong-motion accelerograms: Needs, options and consequences, *Soil Dynam. Earthq. Eng.* **25,** no. 2, 93–115.

Chang, Z., X. Sun, C. Zhai, J. X. Zhao, and L. Xie (2016). An improved energy-based approach for selecting pulse-like ground motions, *Earthq. Eng. Struct. Dynam.* **45,** no. 14, 2405–2411.

Chioccarelli, E., and I. Iervolino (2010). Near-source seismic demand and pulse-like records: A discussion for L'Aquila earthquake, *Earthq. Eng. Struct. Dynam.* **39,** no. 9, 1039–1062, doi: 10.1002/eqe.987.

Chioccarelli, E., and I. Iervolino (2013). Near-source seismic hazard and design scenarios, *Earthq. Eng. Struct. Dynam.* **42,** no. 4, 603–622, doi: 10.1002/eqe.2232.

Cork, T. G., J. H. Kim, G. P. Mavroeidis, J. K. Kim, B. Halldorsson, and A. S. Papageorgiou (2016). Effects of tectonic regime and soil conditions on the pulse period of near-fault ground motions, *Soil Dynam. Earthq. Eng.* **80,** 102–118.

Dreger, D., G. Hurtado, A. Chopra, and S. Larsen (2011). Near-field across-fault seismic ground motions, *Bull. Seismol. Soc. Am.* **101,** no. 1, 202–221.

Fayjaloun, R., M. Causse, C. Voisin, C. Cornou, and F. Cotton (2017). Spatial variability of the directivity pulse periods observed during an earthquake, *Bull. Seismol. Soc. Am.* **107,** 308–318.

Hayden, C. P., J. D. Bray, and N. A. Abrahamson (2014). Selection of near-fault pulse motions, *J. Geotech. Geoenvir. Eng.* **140,** no. 7, 04014030, doi: 10.1061/(ASCE)GT.1943-5606.0001129.

Hayes, G. (2010). Updated result of the Sep 3, 2010 M_w 7.0 Darfield, South Island New Zealand earthquake, available at http://equake-rc.info/SRCMOD/searchmodels/viewmodel/s2010DARFIE01HAYE/ (last accessed May 2021).

Houtte, C. V., S. Bannister, C. Holden, S. Bourguignon, and G. McVerry (2017). The New Zealand Strong Motion Database, *Bull. New Zeal. Soc. Earthq. Eng.* **50,** no. 1, 1–20, doi: 10.5459/bnzsee.50.1.1-20.

Ji, K., Y. Ren, R. Wen, and C. H. Kuo (2019). Near-field velocity pulse-like ground motions on February 6, 2018 M_w 6. 4 Hualien, Taiwan earthquake and structural damage implications, *Soil Dynam. Earthq. Eng.* **126,** 105,784, doi: 10.1016/j.soildyn.2019.105784.

Kamai, R., N. Abrahamson, and R. Graves (2014). Adding fling effects to processed ground-motion time histories, *Bull. Seismol. Soc. Am.* **104,** no. 4, 1914–1929, doi: 10.1785/0120130272.

Kanamori, H., L. Ye, B.-S. Huang, H.-H. Huang, S.-J. Lee, W.-T. Liang, Y.-Y. Lin, K.-F. Ma, Y.-M. Wu, and T.-Y. Yeh (2017). A strong-motion hot spot of the 2016 Meinong, Taiwan, earthquake (M_w 6.4), *Terr. Atmos. Ocean. Sci.* **28,** 637–650.

Kobayashi, H., K. Koketsu, and H. Miyake (2017). Rupture processes of the 2016 Kumamoto earthquake sequence: Causes for extreme ground motions, *Geophys. Res. Lett.* **44,** 6002–6010, doi: 10.1002/2017GL073857.

Kuo, C. H., S. H. Chao, C. C. Hsu, and X. M. Lu (2019). Database of near-fault pulse-like time history, *Technical Report of National Center for Research on Earthquake Engineering*, NCREE-19-010, 137 pp.

Kuo, C. H., J. Y. Huang, C. M. Lin, T. Y. Hsu, S. H. Chao, and K. L. Wen (2019). Strong ground motion and pulse-like velocity observations in the near-fault region of the 2018 M_w 6.4 Hualien, Taiwan, earthquake, *Seismol. Res. Lett.* **90,** 40–50.

Lee, S. J., T. C. Lin, T. Y. Liu, and T. P. Wong (2019). Fault-to-fault jumping rupture of the 2018 M_w 6.4 Hualien earthquake in eastern Taiwan, *Seismol. Res. Lett.* **90,** 30–39.

Lee, S. J., T. Y. Yeh, and Y. Y. Lin (2016). Anomalously large ground motion in the 2016 M_L 6.6 Meinong, Taiwan, earthquake: A synergy effect of source rupture and site amplification, *Seismol. Res. Lett.* **87,** 1319–1326.

Lin, Y. Y., H. Kanamori, Z. Zhan, K. F. Ma, and T. Y. Yeh (2020). Modeling of pulse-like velocity ground motion during the 2018 M_w 6.3 Hualien earthquake, Taiwan, *Geophys. J. Int.* **223,** no. 1, 348–365.

Lin, Y. Y., T. Y. Yeh, K. F. Ma, T. R. A. Song, S. J. Lee, B. S. Huang, and Y. M. Wu (2018). Source characteristics of the 2016 Meinong (M_L 6.6), Taiwan, earthquake, revealed from dense seismic arrays: Double sources and pulse-like velocity ground motion, *Bull. Seismol. Soc. Am.* **108,** 188–199.

Liu, K. S., and Y. B. Tsai (2005). Attenuation relationships of peak ground acceleration and velocity for crustal earthquakes in Taiwan, *Bull. Seismol. Soc. Am.* **95,** no. 3, 1045–1058.

Liu, K. S., T. C. Shin, and Y. B. Tsai (1999). A free-field strong motion network in Taiwan: TSMIP, *Terr. Atmos. Ocean. Sci.* **10,** no. 2, 377–396.

Mena, B., and P. M. Mai (2011). Selection and quantification of near-fault velocity pulses owing to source directivity, *Georisk* **5,** 25–43.

Pacor, F., C. Felicetta, L. Giovanni, S. Sgobba, R. Puglia, M. D'Amico, and I. Iervolino (2018). NESS1: A worldwide collection of strong motion data to investigate near-source effects, *Seismol. Res. Lett.* **89,** no. 6, 2299–2313.

Shahi, S. K., and J. W. Baker (2011). An empirically calibrated framework for including the effects of near-fault directivity in probabilistic seismic hazard analysis, *Bull. Seismol. Soc. Am.* **101,** 742–755.

Shahi, S. K., and J. W. Baker (2014). An efficient algorithm to identify strong-velocity pulses in multicomponent ground motions, *Bull. Seismol. Soc. Am.* **104,** 2456–2466.

Sharbati, R., R. Rahimi, M. R. Koopialipoor, N. Elyasi, F. Khoshnoudian, H. R. Ramazi, and H. R. Amindavar (2020). Detection and extraction of velocity pulses of near-fault ground motions using asymmetric Gaussian Chirplet model, *Soil Dynam. Earthq. Eng.* **133,** 106,123, doi: 10.1016/j.soildyn.2020.106123.

Somei, K., K. Miyakoshi, K. Yoshida, S. Kurahashi, and K. Irikura (2020). Near-source strong pulses during two large M_{JMA} 6.5 and M_{JMA} 7.3 events in the 2016 Kumamoto, Japan, earthquakes, *Pure Appl. Geophys.* **177,** 2223–2240.

Somerville, P., K. Irikura, R. Graves, S. Sawada, D. Wald, N. Abrahamson, Y. Iwasaki, T. Kagawa, N. Smith, and A. Kowada (1999). Characterizing crustal earthquake slip models for the prediction of strong ground motion, *Seismol. Res. Lett.* **70,** no. 1, 59–80, doi: 10.1785/gssrl.70.1.59.

Somerville, P. G. (2003). Magnitude scaling of the near fault rupture directivity pulse, *Phys. Earth Planet. In.* **137,** 201–212.

Somerville, P. G., N. F. Smith, R. W. Graves, and N. A. Abrahamson (1997). Modification of empirical strong ground motion attenuation relations to include the amplitude and duration effects of rupture directivity, *Seismol. Res. Lett.* **68,** no. 1, 199–222.

Tarbali, K., B. A. Bradley, and J. W. Baker (2019). Ground motion selection in the near-fault region considering directivity-induced pulse effects, *Earthq. Spectra* **35,** no. 2, 759–786, doi: 10.1193/102517EQS223M.

von Specht, S. (2019). ICBM—Integrated combined baseline modification: An algorithm for segmented baseline estimation, *Seismol. Res. Lett.* **91,** 475–487, doi: 10.1785/0220190134.

Wang, R., B. Schurr, C. Milkereit, Z. Shao, and M. Jin (2011). An improved automatic scheme for empirical baseline correction of digital strong-motion records, *Bull. Seismol. Soc. Am.* **101,** no. 5, 2029–2044.

Zhu, L., and L. A. Rivera (2002). A note on the dynamic and static displacements from a point source in multilayered media, *Geophys. J. Int.* **148,** 619–627.

APPENDIX

To analyze only pulses generated by wave interference, we develop a strategy to separate the two phenomena from the observations. We perform the static-offset correction described in von Specht (2019) to all recordings to extract the static offset from those pulses. The comparison of the waveforms before and after the static-offset corrections at stations with significant static offsets for the 2016 Kumamoto mainshock is shown in Figure A1.

Kamai *et al.* (2014) evaluated the mean and standard deviation of the period and amplitude of the fling step from observations and simulations. The comparison of their model to our results is shown in Figure A2.

To check the pulse characteristics in the near-field on the relation to variable rupture velocities, the simulations of variable rupture velocities on the fault planes have been computed and show in Figure A3.
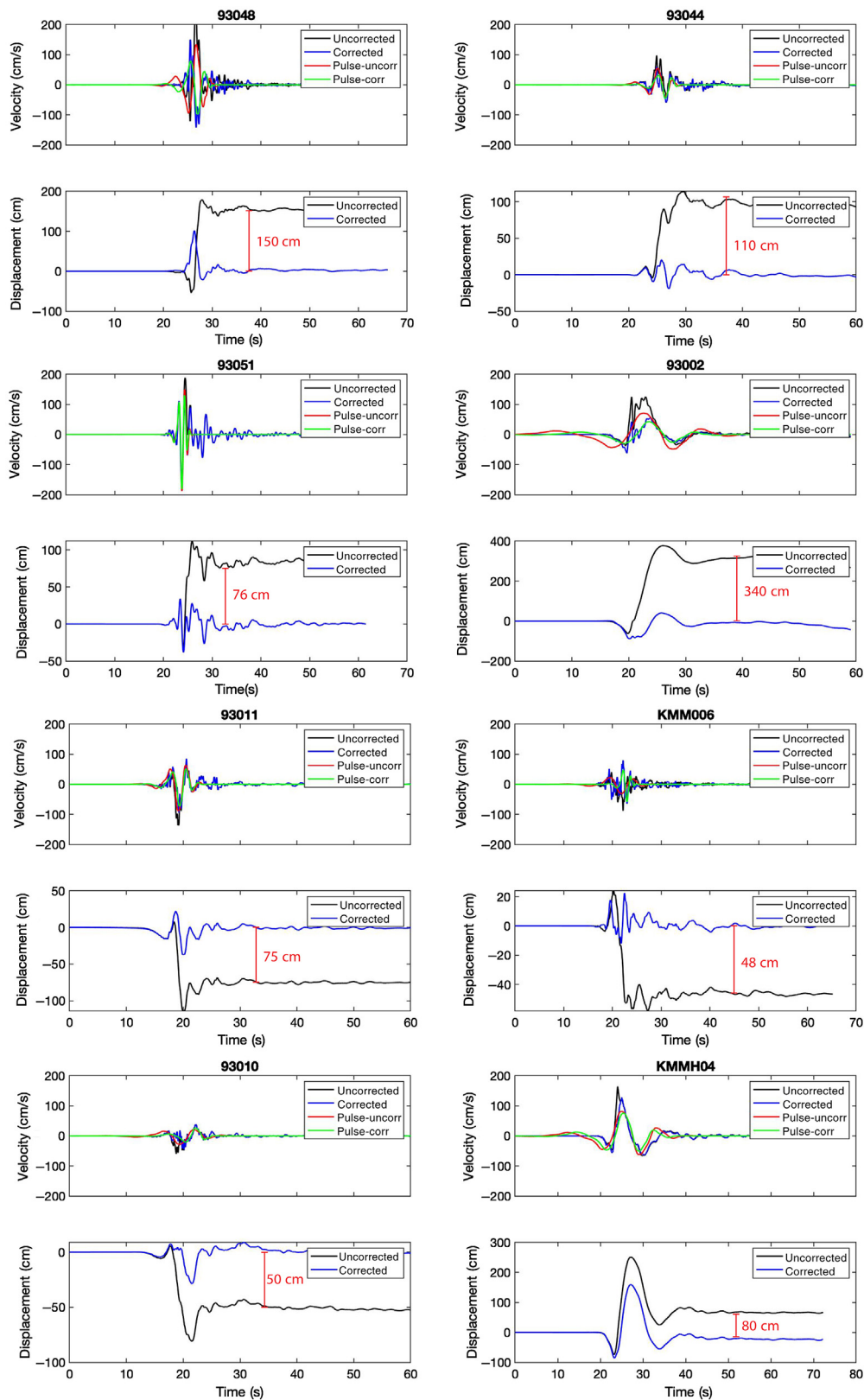
Figure A1. Comparison of waveforms from the 2016 Kumamoto mainshock before and after the static-offset removal. Black curves represent the rotated velocity and displacement at the orientation of the pulse before the static-offset removal. Blue curves represent the rotated velocity and displacement at the orientation of the pulse after the static-offset removal. Red curves represent the extracted pulses before the static-offset removal by the method of Shahi and Baker (2014). Green curves represent the extracted pulses after the static-offset removal by the method of Shahi and Baker (2014). The color version of this figure is available only in the electronic edition.
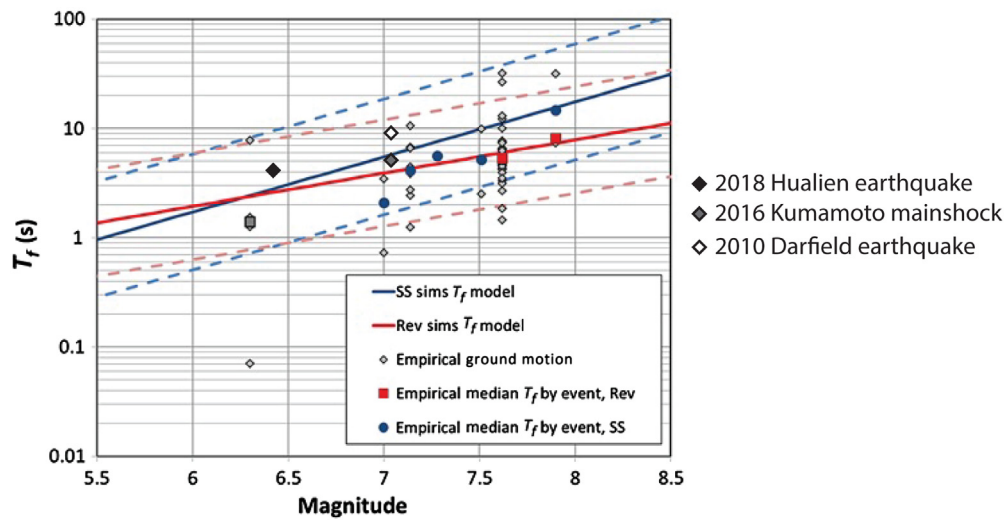
Figure A2. Scaling of the fling pulse period with magnitude (figure revised from figure 11 in Kamai *et al.*, 2014). The color version of this figure is available only in the electronic edition.
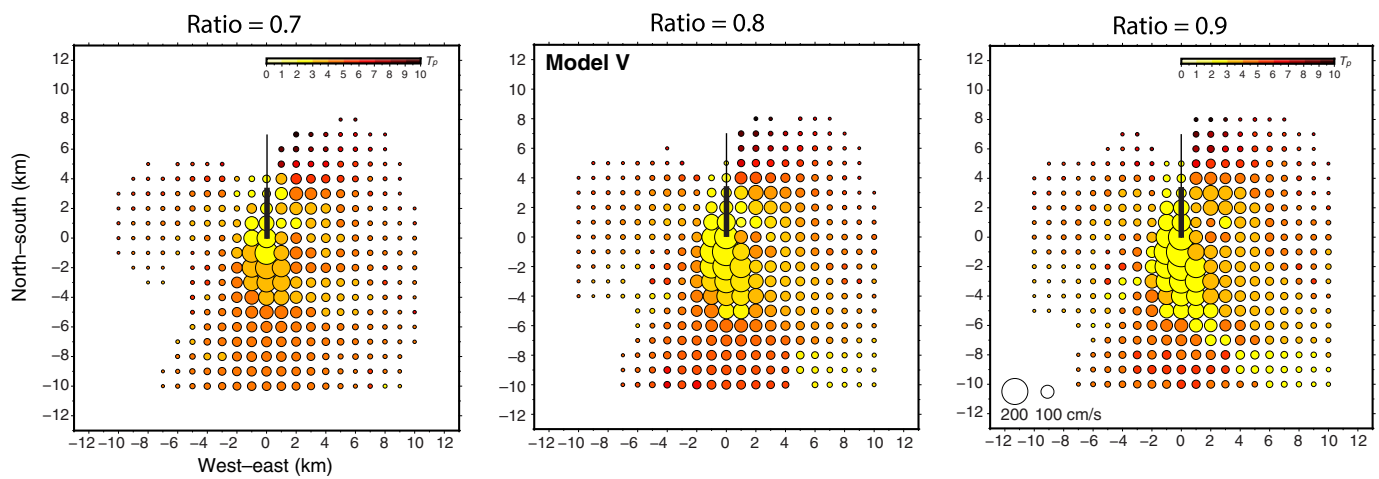

Figure A3. Impact of the rupture speed on pulses periods and amplitudes. The circle color represents the pulse period, and the size of circles represents the pulse velocity. The settings of model V is shown in Figure 7. The color version of this figure is available only in the electronic edition.